ISSN 2712-8008
Том / Volume 26 №2 2026
Домашняя страница журнала: http://vestnik.pstu.ru/geo/
НЕДРОПОЛЬЗОВАНИЕ

УДК 622.276.3
Статья / Article
© ПНИПУ / PNRPU, 2026

Mass-Based Modeling of Submicron Particle-Induced Clogging in Porous Media

Evgenii V. Kozhevnikov, Aleksandr A. Shcherbakov, Zakhar G. Ivanov,
Dmitriy V. Kobyakov, Galina V. Tyurina, Anton P. Petrovykh, Aleksei G. Parshakov
Perm National Research Polytechnic University (29 Komsomolskiy av., Perm, 614990, Russian Federation)

Моделирование кольматации пористой среды субмикронными частицами

Е.В. Кожевников, А.А. Щербаков, З.Г. Иванов, Д.В. Кобяков, Г.В. Тюрина, А.П. Петровых, А.Г. Паршаков
Пермский национальный исследовательский политехнический университет (Российская Федерация, 614990, г. Пермь, Комсомольский пр., 29)

Получена / Received: 01.11.2025. Принята / Accepted: 20.04.2026. Опубликована / Published: 14.05.2026

Keywords:
water injection, permeability, suspended solids, particle retention, pore clogging.

Water injection into hydrocarbon reservoirs is routinely accompanied by the entrainment of suspended solids, and the most problematic fraction is sub-micron (< 1 μm) particulate matter that is difficult to remove by conventional gravity treatment and can progressively impair injectivity by clogging pore constrictions. We investigated nanoparticle-driven permeability degradation using vertical quartz sand packs (column diameter 24 mm, height 0.20 m) with two sand fractions (0.316–0.20 and 0.20–0.10 mm) and two particle types: TiO_2 (≈ 200 nm) and WO_3 (≈ 80–100 nm). Permeability was evaluated from Darcy's law and analyzed as a function of cumulative injected mass, including the specific injected mass (mass per cross-sectional area). Across all runs, k(m) exhibits a rapid, quasi-linear decline at low mass followed by a weak-sensitivity plateau at late stages, indicating progressive redistribution of flow pathways and approach to a dynamic deposition–release regime. Finer sands clogged at substantially lower cumulative mass than coarser sands, consistent with smaller characteristic throat radii, whereas the smaller WO_3 particles required a larger specific mass to reach comparable permeability loss, reflecting deeper penetration. Post-experiment sectioning revealed strongly inlet-biased retention profiles with maximum deposit load in the upper centimeters. A discrete 5-mm layered model was developed, coupling layer-wise retention, porosity loss, and a Kozeny–Carman closure with hydraulic resistances in series; parameters were identified by simultaneously matching permeability–mass curves and retained-mass profiles. The resulting framework provides a mass-based scaling variable for transferring laboratory clogging trends to near-wellbore impairment in injection and recharge wells.

Ключевые слова:
закачка воды, проницаемость, взвешенные частицы, удержание частиц, кольматация порового пространства.

Закачка загрязненных вод в нефтегазовые пласты воды с целью поддержания пластового давления может сопровождаться поступлением в пласт взвешенных механических примесей. Наиболее проблемной является субмикронная фракция (менее 1 мкм), которая трудно удаляется стандартными методами подготовки и способна вызывать прогрессирующее снижение приемистости нагнетательных скважин за счет закупоривания пор. В работе исследовано снижение проницаемости, обусловленное задержанием субмикронных частиц, на вертикальных кварцевых песчаных моделях пористой среды (диаметр 24 мм, высота 0,20 м) при использовании двух фракций песка (0,316–0,20 и 0,20–0,10 мм) и двух типов частиц с характерным размером около 100 и 200 нм. Проницаемость определяли по закону Дарси и анализировали в зависимости от накопленной массы закачанных частиц. Установлено, что на начальном этапе закачки проницаемость снижается быстро, после чего процесс переходит в стадию слабой изменчивости, что соответствует формированию устойчивых путей фильтрации и приближению системы к динамическому равновесию между задержанием и выносом частиц. Для более мелкой фракции песка снижение проницаемости наступает при меньшей накопленной массе, что согласуется с меньшими характерными размерами пор. Для более мелких частиц сопоставимое снижение проницаемости достигается при большей накопленной массе, что указывает на более глубокое проникновение и распределение частиц в объеме модели. Профили распределения удержанной массы по длине характеризуются максимальной концентрацией частиц в начале модели. Для интерпретации результатов разработана дискретная послойная модель с шагом 5 мм, учитывающая задержание частиц по слоям, уменьшение пористости и связь между пористостью и проницаемостью по уравнению Козени — Кармана при последовательном суммировании гидравлических сопротивлений слоев; параметры модели определяли по согласованию экспериментальных зависимостей проницаемости от накопленной массы и профилей удержанной массы. Полученные результаты могут быть использованы для оценки снижения приемистости при закачке загрязненных вод.

Evgenii V. Kozhevnikov (Author ID in Scopus: 55531698200, ORCID: 0000-0002-6084-0795) – PhD, e-mail: kev@pstu.ru. The contact person for correspondence.
Aleksandr A. Shcherbakov (Author ID in Scopus: 55531112100, ORCID: 0000-0001-6502-970X), e-mail: aashherbakov@pstu.ru.
Zakhar G. Ivanov (Author ID in Scopus: 59022877200, ORCID: 0009-0001-7957-8280), e-mail: zakharivanov@pstu.ru.
Dmitriy V. Kobyakov (ORCID: 0000-0002-0236-6589), e-mail: kev@pstu.ru.
Galina V. Tyurina (ORCID: 0009-0007-9479-310X), e-mail: gvturina@pstu.ru.
Anton P. Petrovykh (ORCID: 0009-0003-1279-3183), e-mail: kev@pstu.ru.
Aleksei G. Parshakov (ORCID: 0009-0003-2898-5091), e-mail: kev@pstu.ru.

Кожевников Евгений Васильевич (Author ID in Scopus: 55531698200, ORCID: 0000-0002-6084-0795) – кандидат технических наук, e-mail: kev@pstu.ru. Контактное лицо для переписки.
Щербаков Александр Анатольевич (Author ID in Scopus: 55531112100, ORCID: 0000-0001-6502-970X), e-mail: aashherbakov@pstu.ru.
Иванов Захар Григорьевич (Author ID in Scopus: 59022877200, ORCID: 0009-0001-7957-8280), e-mail: zakharivanov@pstu.ru.
Кобяков Дмитрий Вадимович (ORCID: 0000-0002-0236-6589), e-mail: kev@pstu.ru.
Тюрина Галина Вячеславовна (ORCID: 0009-0007-9479-310X), e-mail: gvturina@pstu.ru.
Петровых Антон Павлович (ORCID: 0009-0003-1279-3183), e-mail: kev@pstu.ru.
Паршаков Алексей Григорьевич (ORCID: 0009-0003-2898-5091), e-mail: kev@pstu.ru.

Просьба ссылаться на эту статью в русскоязычных источниках следующим образом:
Моделирование кольматации пористой среды субмикронными частицами / Е.В. Кожевников, А.А. Щербаков, З.Г. Иванов, Д.В. Кобяков, Г.В. Тюрина, А.П. Петровых, А.Г. Паршаков // Недропользование. – 2026. – Т. 26, № 2. – С. 123–133. DOI: 10.15593/2712-8008/2026.2.5

Please cite this article in English as:
Kozhevnikov E.V., Shcherbakov A.A., Ivanov Z.G., Kobyakov D.V., TyurinaG.V., Petrovykh A.P., Parshakov A.G. Mass-Based Modeling of Submicron Particle-Induced Clogging in Porous Media. Perm Journal of Petroleum and Mining Engineering, 2026, vol. 26, no. 2, pp. 123–133. DOI: 10.15593/2712-8008/2026.2.5

Introduction

Water injection is a core element of pressure-maintenance waterflooding in hydrocarbon reservoirs [1]. In field operations, it is frequently managed as a support activity with limited direct revenue attribution; therefore, operational control tends to prioritise meeting target injection rates and volumes, while injection-water quality is often treated as secondary [2].

The quality of produced water re-injected into the reservoir is determined primarily by residual hydrocarbons and suspended solids. Suspended solids are typically the dominant constraint for water treatment and injectivity management. Particles can accumulate within surface facilities and downhole components (flowlines, wellbore, and perforations) and can induce near-wellbore formation damage through pore-throat plugging and permeability impairment. This increases operational complexity and reduces the effective flow capacity of the near-wellbore zone [3–5].

The most challenging fraction comprises submicron solids (<1 μm), commonly including fine mineral particles (clays), inorganic salts, and corrosion products generated within the production and injection system [6, 7]. Conventional gravity separation used in many fields removes this fraction only with substantially increased residence time and, consequently, larger equipment footprints [8]. Under practical constraints, a significant proportion of submicron solids remains in the injected water and is transported into the formation [9,10].

Due to their small size, submicron particles may penetrate beyond the immediate near-wellbore region and promote distributed plugging, rather than purely localised impairment. This mechanism is consistent with the gradual decline in injectivity observed during long-term injection operations [11, 12]. Field evidence also supports the role of solids: in some cases, siltation within injection intervals is indicated by the inability to run logging tools below the lowest perforations, which implies mechanical blockage in the near-wellbore region.

In engineering practice, water-treatment specifications are commonly defined by allowable suspended-solids concentrations. However, even when injected water meets nominal standards, prolonged injection can still result in progressive solids accumulation in the near-wellbore zone and associated formation damage [13, 14]. The outcome is reduced injectivity and the requirement for remedial treatments. In addition, near-wellbore plugging can promote preferential flow pathways and channelling, reducing waterflood effectiveness by degrading sweep.

Revision of produced-water treatment requirements therefore requires a quantitative assessment of the impact of suspended solids on near-wellbore flow properties and on injection-well operating performance. This motivates models that relate solids concentration, particle-size distribution, and physicochemical properties of injected particulates to pore-space contamination and permeability reduction. Published approaches include empirical correlations, deep-bed filtration models incorporating attachment/detachment kinetics, and formulations that account for filter-cake development. The following discussion summarises these model classes and evaluates their applicability to produced-water injection containing submicron solids.

Empirical engineering approaches typically correlate permeability decline with time/throughput volume or solids concentration, using effective plugging coefficients calibrated to laboratory or field data. These correlations are useful for screening, but they are often not transferable between assets because they do not isolate the governing capture mechanisms (adhesion, straining, bridging) and do not represent deposit evolution under changing hydrodynamic conditions [15]. Deep-bed filtration models provide a more mechanistic framework by prescribing attachment/detachment kinetics and linking retained mass to permeability loss. For several formulations, analytical solutions and regime criteria have been developed for high-retention conditions, supporting model verification and parameter identification [16]. Probabilistic and pore-network approaches treat particle jamming in pore throats as a stochastic process controlled by local geometry and flow, enabling a structured pathway from pore-scale processes to effective properties at continuum scale [17–19].

For practical water injection, the dominant impairment mechanism may shift between deep retention within the pore volume, straining in constrictions, bridging, and near-surface cake growth. Pore-scale and microfluidic studies demonstrate how individual particles and aggregates initiate blockage growth and redistribute flow, and they report nonlinear dependence of plugging rate on filtration velocity and solids supply conditions [20–23]. These insights are valuable, but direct parameter transfer to reservoir rocks is limited by differences between idealised microchannel geometries and natural pore structures, and by scale effects including pore-size distributions, heterogeneity, cementation, and clay content [24, 25]. Tomography-supported pore-scale modelling has been used to reconstruct particle pathways and identify blockage locations, improving mechanistic interpretation; however, these methods remain computationally intensive and require upscaling assumptions for near-wellbore applications [26, 27]. In waterflooding for pressure maintenance, additional coupled processes may be material, including poroelastic stress redistribution affecting permeability independently of solids [17], as well as thermo-hydrodynamic and rock-specific effects (e.g., geothermal settings) that alter particle stability and particle–rock interactions [28–30].

Physicochemical conditions (ionic strength, pH, and water composition) influence electrostatic interactions and thereby control colloid retention and remobilisation; changes in pH can shift the system from stable deposition to particle release and partial permeability recovery [31]. For fresh-water injection scenarios, these effects may be treated as fixed boundary conditions, but the assumption should be stated explicitly because many studies address brackish/reactive waters and/or biological plugging, where biofilm growth and biogeochemistry (including iron cycling) can dominate [26, 32].

Most published models and experiments focus on migration of native colloids initially present in the rock at a prescribed concentration [15, 33]. In contrast, produced-water injection for pressure maintenance is characterised by a long-term, sustained influx of external submicron particles delivered with injected water. For this regime, it is essential to track the cumulative injected solids mass and its spatial distribution within the pore space (from the near-wellbore region into the formation), including potential transitions from deep-bed filtration to cake-dominated behaviour as flow rate and particle-size distribution vary [20–22]. The novelty of the present work is the use of a mass-balance framework as the primary descriptor of solids

loading and the establishment, based on experimental data, of a quantitative relationship between accumulated particle mass and degradation of near-wellbore flow properties, providing a basis for calculation-driven justification of produced-water treatment requirements.

Theoretical framework for modelling pore–space clogging during injection of contaminated water

In studies of pore-space clogging associated with the transport of fine suspended matter, most models are formulated by coupling particle transport in the flowing phase with retention within the porous matrix, followed by an update of the resulting flow properties. The prevailing baseline framework is the continuum deep-bed filtration formulation, in which the mass concentration of particles in the aqueous phase, $C(x,t)$ (kg/m^3), defined along the spatial coordinate x(m) and time t(s), is governed by a convection–dispersion balance with an additional retention term $R(C,S)$. Similar formulations are widely used in studies of clogging development during suspension filtration and in investigations of fines/colloid migration in porous media [16, 22, 23, 28]. In one-dimensional form, the governing equation is written as:

$$\frac{\partial(\phi C)}{\partial t}+\frac{\partial(uC)}{\partial x}=\frac{\partial}{\partial x};\left(\phi D\frac{\partial C}{\partial x}\right)-R(C,S), \quad (1)$$

where ϕ is porosity, u is the Darcy (superficial) velocity, and D is the dispersion coefficient. The accumulation of retained particles is represented by the variable $S(x,t)$ (mass of deposited solids per unit bulk volume of porous medium) and described by the following balance equation:

$$\frac{\partial S}{\partial t}=R(C,S). \quad (2)$$

Within this general framework, the differences between individual models are primarily determined by the specific functional form of $R(C,S)$. The most widely used option is first-order attachment kinetics with respect to concentration:

$$R=k_aC, \quad (3)$$

where k_a is the attachment (capture) coefficient. This expression is commonly used as a baseline approximation in deep-bed filtration models and can be refined as required [16,28]. To account for remobilisation, a detachment term is introduced, yielding an attachment–detachment formulation:

$$R=k_aC-k_dS, \quad (4)$$

where k_d is the detachment coefficient. The dependence of these parameters on flow regime and injection history is discussed in studies addressing the effects of filtration velocity and initial conditions on clogging evolution [22, 23]. To represent a finite retention capacity, a maximum retained mass S_{max} is introduced and a saturating kinetic law is used:

$$R=k_aC\left(1-\frac{S}{S_{max}}\right)-k_dS, \quad (5)$$

which allows the model to reproduce the progressive reduction in capture as available retention sites become occupied and to represent transitions between process stages. Formulations in the high-retention limit and their analytical solutions are discussed in the literature on nonlinear retention models [16]. Where capture exhibits pronounced nonlinearity (for example, due to aggregation or cooperative growth), a power-law dependence on concentration is employed:

$$R=kC^n\left(1-\frac{S}{S_{max}}\right), \quad (6)$$

where k is a coefficient and n is the power-law exponent [16].

Mechanical retention in pore throats (straining/bridging) is commonly incorporated within the continuum framework as an additional retention contribution:

$$R=R_{att}+R_{str}, \quad (7)$$

where R_{att} denotes the contribution from adhesive attachment and R_{str} represents the contribution from mechanical retention. To include straining, a size-ratio threshold is typically applied: for a characteristic particle (or aggregate) size d_p(m) and a characteristic pore-throat size d_t(m), straining is activated when $(d_p/d_t)\geq\lambda$, where λ is a dimensionless threshold. One widely used formulation is written as:

$$R_{str}=k_sH;\left(\frac{d_p}{d_t}\right)C, \quad (8)$$

where k_s is the mechanical retention coefficient (1/s) and H is the Heaviside step function. Bridging mechanisms and the role of constriction geometry have been examined in detail using micromodel and microfluidic experiments; however, transferring the corresponding parameters to natural pore networks generally requires dedicated calibration [21, 24, 27].

To translate retained mass into changes in flow properties, models introduce a deposit–porosity/permeability relationship. If S is defined as deposited mass per unit bulk volume of porous medium, porosity can be expressed as:

$$\phi=\phi_0-\frac{S}{\rho_s}, \quad (9)$$

where ϕ_0 is the initial porosity and ρ_s is the density of the solid phase. A Kozeny–Carman-type relationship is then applied for permeability (k^2):

$$k=k_0\left(\frac{\phi}{\phi_0}\right)^3\left(\frac{1-\phi_0}{1-\phi}\right)^2, \quad (10)$$

where k_0 is the initial permeability. Alternatively, a simpler exponential relationship can be used to relate permeability directly to retained mass:

$$k=k_0\exp(-\beta S), \quad (11)$$

where β is a parameter identified from data. Closure relations of this type are widely used in practical descriptions of permeability degradation in particle retention/migration models [16, 28]. Structural factors controlling the form of $k(S)$ are also discussed, including the effects of polydispersity and the deformability of the packed deposit layer [19], as well as coupling with poroelastic response during injection [17].

Where near-surface accumulation dominates, a cake filtration concept is applied by introducing an additional hydraulic resistance R_c (1/m) into the pressure-drop relationship ΔP (Pa). For viscosity μ (Pa·s), Darcy velocity u (m/s), and a characteristic zone length L:

$$\Delta P=\mu u\left(\frac{L}{k}+R_c\right), \quad (12)$$

and the growth of cake mass $M_c(t)$ (kg), for a flow rate $Q(t)$ (m^3/s) and an inlet particle concentration $C_{in}(t)$ (kg/m^3), is described as:

$$\frac{dM_c}{dt}=\eta_cQC_{in}, \quad (13)$$

where η_c is the fraction of particles contributing to cake formation. The cake resistance is related to cake mass via the specific cake resistance α_c and the filtration area A:

$$R_c = \alpha_c \frac{M_c}{A}, \quad (14)$$

At the microscale, the mechanisms governing cake growth and deposit structure have been investigated both for suspension filtration and for progressive plugging (including dendritic growth). These studies are used to justify the choice of α_c and to define criteria for the transition to a cake-dominated regime [20, 21].

For water injection, the key condition is a sustained flow of water carrying submicron particles, typically at a quasi-constant low concentration. Accordingly, a mass-based descriptor is introduced to represent the pore-blocking mechanism. The inlet particle mass flow rate $\dot{M}_{in}(t)$ is defined as $\dot{M}_{in}(t) = Q(t)C_{in}(t)$, and the cumulative injected mass $M_{in}(t)$ is obtained by integration:

$$M_{in}(t) = \int_0^t Q(t)C_{in}(t)dt. \quad (15)$$

Similarly, the cumulative produced (exported) mass $M_{out}(t)$ is defined using the outlet concentration $C_{out}(t)$:

$$M_{out}(t) = \int_0^t Q(t)C_{out}(t)dt \quad (16)$$

and the retained (accumulated) mass is defined as:

$$M_{ret}(t) = M_{in}(t) - M_{out}(t) \quad (17)$$

For a porous-medium control volume V, the specific retention is expressed as:

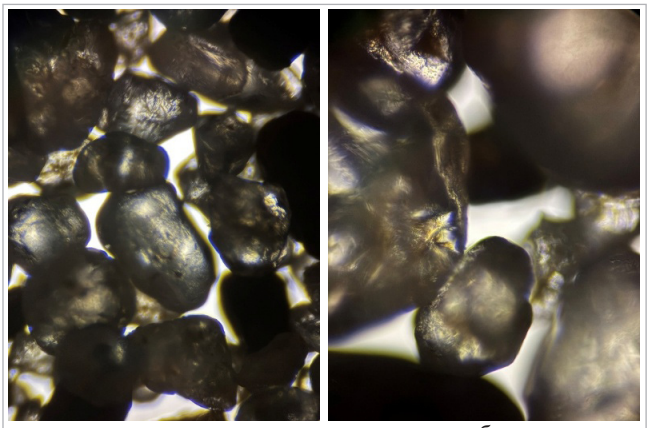
$$S(t) = \frac{M_{ret}(t)}{V} \quad (18)$$

after which the permeability $k(t)$ is evaluated using the selected $k(S)$ closure via (10) or (11). This shift to a mass-based formulation is consistent with the fact that many studies focus on the evolution of C/C_0 and k/k_0 under a prescribed inlet concentration, whereas long-term injection requires relationships referenced to the cumulative inflow of solids. In this context, the effects of filtration velocity and injection start-up conditions on plugging development can be represented through the dependence of k_a, k_d, S_{max}, k_s, and η_c on operating regime variables u and Q [22, 23]. It should also be noted that physicochemical factors (salinity, pH) are often incorporated through their influence on attachment/detachment coefficients; for fresh-water injection, these parameters may be treated as constant and represented by fixed values [28, 34].

Methodology

In the experiments, the model porous medium was a washed quartz sand that was dried and sieved using a 0.316×0.316 mm mesh (Fig. 1). The fraction finer than 0.1 mm accounts for less than 0.2 %, which minimises the likelihood of intergranular voids being filled by a fine fraction. The characteristic grain sizes are $D_{10} \approx 0.16$ mm, $D_{50} \approx 0.29$ mm, and $D_{90} \approx 0.40$ mm. The Sauter mean diameter calculated from the particle-size distribution is $d_{32} \approx 0.26$ mm.

The sand pack was treated as a randomly packed, unconsolidated granular medium with a characteristic porosity of $\phi \approx 0.35$–0.40, typical of medium- to coarse-grained sands. The pore space is represented by an interconnected system of pore bodies and constrictions (pore throats) formed at contacts between grains of varying size and shape.



а *б*

Fig. 1. Micrographs of the washed sand used in this study; magnification: 400× (*a*), 800× (*b*)

For a quantitative description of flow properties, the classical Kozeny–Carman-type relationship was used, linking permeability to porosity and the specific surface area of the solid phase:

$$k = \frac{\varphi^3}{C_K S^2 (1-\varphi)^2}, \quad (19)$$

where k is the absolute permeability, S is the specific surface area of the grains, and C_K is the empirical Kozeny–Carman constant. The modern form of the equation and its applicability to granular media are discussed in detail in [35] and [36].

The specific surface area of the sand was estimated using the Sauter mean diameter:

$$S = \frac{6}{d_{32}}, \quad (20)$$

which is a standard approximation for granular media within the Kozeny–Carman framework and is adopted in modern reviews and filtration models [35].

The mean hydraulic radius of the pore space, defined as the ratio of pore volume to wetted surface area, was estimated using:

$$r_h = \frac{\varphi d_{32}}{6(1-\varphi)}, \quad (21)$$

thereby linking pore-space geometry to the flow characteristics of the medium. For the sand investigated, typical values of r_h are on the order of 20–30 μm.

The minimum pore-space cross-sections (pore throats), which control most of the hydraulic resistance, have a characteristic radius $r_t \approx 15$–25 μm, corresponding to an equivalent diameter of 30–50 μm. The pore bodies connected by the throat network have an equivalent size of approximately 60–150 μm. The characteristic length of a pore channel between adjacent throats is comparable to the median grain size and is approximately 0.15–0.30 mm. The actual flow-path length exceeds the geometric distance due to the tortuosity of the pore network, consistent with numerical and experimental estimates for random grain packings [37].

Flow channels are characterised by a variable cross-section. Pore throats are predominantly wedge-shaped or slit-like triangular constrictions, whereas pore bodies are irregular polygonal expansions. This geometry is typical of randomly packed, unconsolidated sands and results in high sensitivity of permeability to changes in porosity and to the structure of intergranular contacts.

The experiments were conducted using a vertical sand pack in a cylindrical column ($D = 24$ mm, bed height 20 cm, mass of the main sand fraction 150 g). The characteristic sizes of the sand packs and injected particles are summarised in Table 1. Permeability k was calculated from Darcy's law using the instantaneous flow rate under a constant imposed head.

Table 1

Characteristic sizes of sand packs and injected particles

№	Sand, mm	d_{50} (estimate), μm	Pore-throat radius r_t, μm	Nano-particles	Particle size, nm
1	0.2–0.1	~150	~8–18	TiO_2	~200
2	0.316–0.2	~250	~15–30	TiO_2	~200
3	0.2–0.1	~150	~8–18	WO_3	~80–100
4	0.316–0.2	~250	~15–30	WO_3	~80–100

Experimental Results

Experimental data yield permeability trends as a function of the cumulative injected particle mass (Fig. 2). Across all test series, $k(m)$ exhibits a consistent pattern: permeability decreases as m increases until low values are reached, followed by a region of weak sensitivity (an approximate plateau) in which further increases in injected mass have little effect on the overall transmissibility of the sand pack.

The shape of the curves reflects a progressive reorganisation of the conducting pathways. At low m, the most pronounced—often near-linear—decline in k is associated with the blockage of the most conductive pore throats; subsequently, the decline becomes more gradual as flow redistributes through the remaining pathways. Ultimately, as m accumulates, the medium transitions to a low-permeability state. For the finer sand fraction (0.2–0.1 mm), the reduction in k occurs at lower values of m than for the coarser sand (0.316–0.2 mm), i.e. the finer pack clogs more rapidly on a cumulative-mass basis. This is consistent with smaller characteristic pore-throat dimensions. For a given sand grade, a larger nanoparticle mass m is required to reach the low-permeability regime.

Profiles of retained-particle distribution along the height of the sand packs were constructed (Fig. 3). The vertical profile of retained solids exhibits a clear maximum in the upper part of the bed and decreases with depth. This indicates preferential development of a near-inlet zone with elevated hydraulic resistance. It was also observed that smaller particles are retained closer to the inlet and penetrate less deeply into the porous medium. An example of internal filter-cake formation at the inlet of the sand pack is shown in the photographs (Fig. 3). The plots also mark, with vertical lines, the periodic stepwise changes in permeability associated with filtration pauses at the end of the working day. During shutdown, pressure within the sand pack equalised and the absence of a pressure gradient promoted partial elastic relaxation/loosening of the deposit layer. As a result, a small permeability increase is observed when filtration is resumed. This effect is most pronounced for TiO_2 suspension filtration in the coarser sand pack (0.316–0.2 mm).

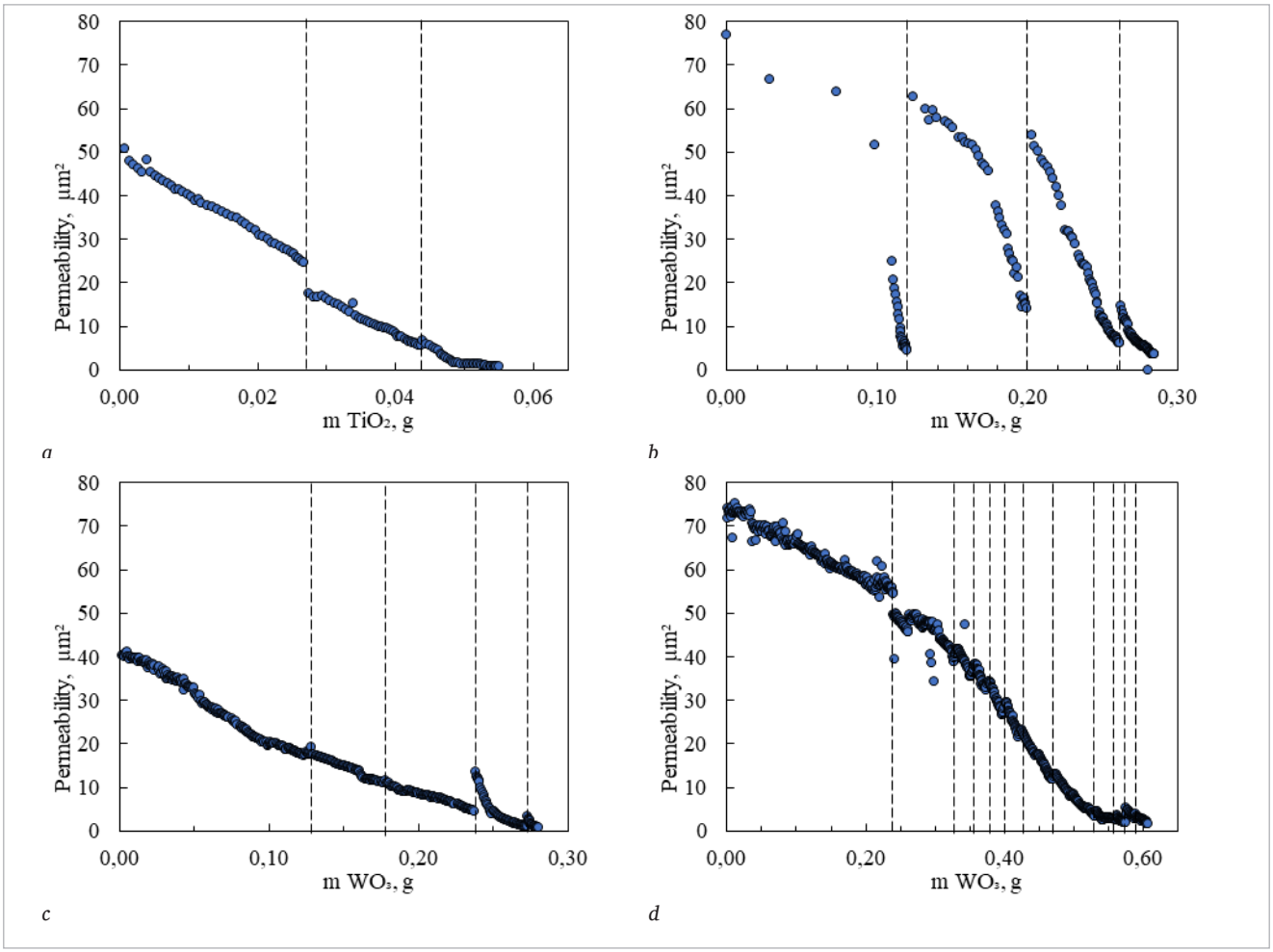


Fig. 2. Effect of cumulative injected particle mass on model permeability for sand grain-size fractions: *a* – 0.2–0.1 mm; *b* – 0.316–0.2 mm; *c* – 0.2–0.1 mm; and *d* – 0.316–0.2 mm. Vertical dashed lines indicate filtration pauses at the end of the work shift

The following characteristic sizes were considered: TiO_2 ~200 nm and WO3 ~80–100 nm. For the 0.316–0.20 mm sand pack, the equivalent pore-throat radius is approximately 15–30 μm, whereas for the 0.20–0.10 mm fraction it is approximately 7–15 μm. Since particle sizes are two to three orders of magnitude smaller than the characteristic throat dimensions, permeability alteration is governed primarily by cumulative mass loading and the effective constriction of hydraulically controlling pore throats.

For the 0.316–0.20 mm sand during TiO_2 filtration, permeability decreases with increasing σ_m towards a terminal value corresponding to $m = 0.284$ g, i.e. $\sigma_m = 0.0628$ g/cm^2 (≈ 0.628 kg/m^2), with a tendency to stabilise at low values at higher σ_m. The retention profile (Fig. 3) indicates that deposition is concentrated in the upper part of the bed (the first few centimetres), consistent with the development of a near-inlet zone of elevated resistance for pore throats on the order of 15–30 μm.

For the same sand grade (pore throats ~15–30 μm) but with WO3 (80–100 nm), permeability degradation is distributed over a substantially larger specific mass loading and reaches a terminal state at $m \approx 0.599$ g, i.e. $\sigma_m = 0.132$ g/cm^2 (≈ 1.324 kg/m^2). Relative to TiO_2, the $k(\sigma_m)$ trend is shifted towards higher σ_m: achieving a comparable permeability reduction requires a higher cumulative solids loading, consistent with deeper migration of the finer particles at an unchanged throat scale.

For the finer 0.20–0.10 mm sand fraction, where characteristic throat radii decrease to 7–15 μm, permeability degradation develops markedly faster with respect to cumulative mass. In the TiO_2 series, the terminal cumulative mass is $m \approx 0.053$ g, i.e. $\sigma_m = 0.0117$ g/cm^2 (≈ 0.117 kg/m^2), at which a pronounced reduction in k is already observed. For WO3 in the same sand fraction, the terminal mass $m \approx 0.110$ g corresponds to $\sigma_m = 0.0243$ g/cm^2 (≈ 0.243 kg/m^2): the $k(\sigma_m)$ curve lies to the right of the TiO_2 case, meaning that a comparable permeability loss requires a higher specific cumulative mass. Nevertheless, the process remains "faster" in terms of σ_m than in the coarser fraction due to the smaller pore-throat size.

Overall, comparison of all series in $k(\sigma_m)$ coordinates shows that reducing the characteristic throat radius when moving from 0.316–0.20 mm to 0.20–0.10 mm sand decreases the σ_m required for a substantial permeability decline. Conversely, reducing particle size when moving from TiO_2 to WO3 shifts the permeability-degradation trend towards higher σ_m for the same porous medium, consistent with deeper migration of the dispersed phase.

Numerical Solution of the Permeability–Degradation Problem During Particle Filtration

This chapter presents a discrete, layer-resolved model that links retention and remobilization of injected nanoparticles inside pore throats to the progressive growth of a near-inlet clogged zone and the resulting evolution of the bulk permeability computed from Darcy's law. The model is designed to reproduce the key experimental observation

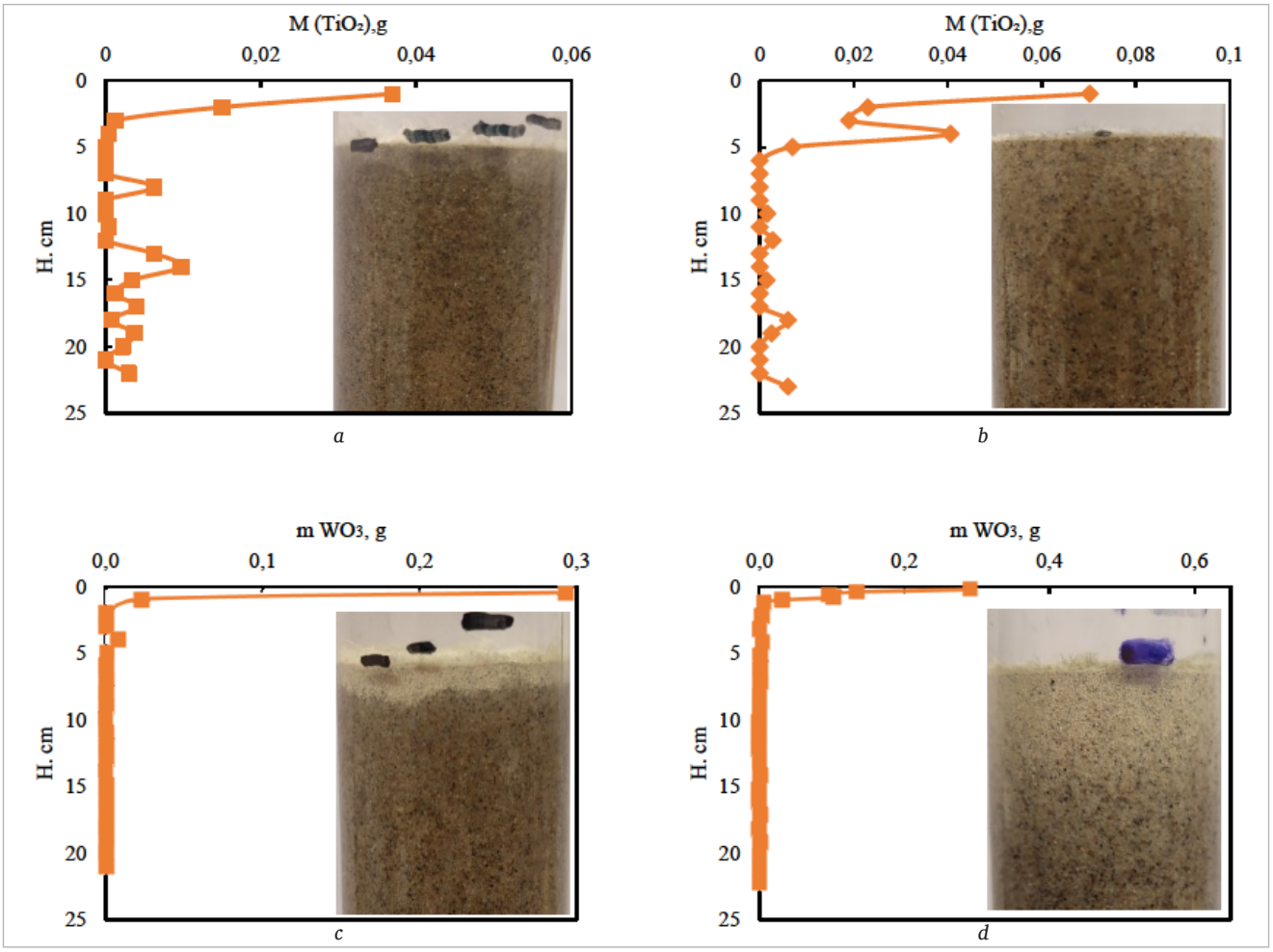


Fig. 3. Appearance of the contaminated section of the sand packs and retained-mass distributions along model height (retention profiles) for sand grain-size fractions: *a* – 0.2–0.1 mm; *b* – 0.316–0.2 mm; *c* – 0.2–0.1 mm, and *d* – 0.316–0.2 mm

from this study: for the tested conditions, permeability is primarily governed by the cumulative injected mass (rather than the instantaneous concentration), and retained particles are concentrated in the upper part of the sand pack, while a quasi-steady (dynamic) regime of deposition–release is reached at late stages.

The porous medium is a vertical cylindrical sand pack of height $H = 0.20$, internal diameter $D = 24$ mm. The sand mass is 150 g. Three granulometric ranges were tested in the experiments described in this work: 0.316–0.20 mm, 0.20–0.10 mm, and an intermediate range depending on the specific run. Two nanoparticle types were injected: TiO_2 (typical primary size ~0.2 μm) and WO_3 (typical size 0.1 μm). For packed sands with these grain sizes, characteristic pore-throat dimensions are on the order of tens of micrometers; a convenient scale estimate follows from Kozeny-type relations between permeability and hydraulic radius (via porosity and specific surface), which are widely used for granular media and provide the geometric bridge needed here [35].

To capture the experimentally observed localization of retained mass near the inlet and the advance of a stable contamination front, the pack is discretized into N horizontal layers of thickness $\Delta z = 5$ mm, so $N = H/\Delta z = 40$. Each layer i (centered at depth z_i) is treated as a locally homogeneous porous slab with its own permeability k_i, porosity ϕ_i, and an effective pore-throat length scale (expressed through hydraulic radius $r_{h,i}$ or an equivalent throat radius $r_{t,i}$). Layers are hydraulically connected in series, so the total pressure drop is the sum of layer pressure drops, and the effective permeability k_{eff} is the harmonic average weighted by Δz.

The model is advanced by the cumulative injected mass, which matches the way the experimental trends collapse: the independent variable is the specific injected mass (mass per cross-sectional area):

$$\sigma_{inj} = \frac{M_{inj}}{A} \tag{22}$$

and all permeability curves are analyzed as $k(\sigma_{inj})$. This is the same variable used to compare different runs and different sands at identical column geometry. In the spreadsheet, σ_{inj} is incremented stepwise ($\Delta\sigma_{inj}$), and each step is distributed over the layers as deposited or transported mass.

For a given step, the volumetric flow rate Q is measured experimentally; the superficial Darcy velocity is $u_D = Q/A$. The permeability of the entire pack is computed from Darcy's law:

$$k_{eff} = \frac{\mu u_D H}{\Delta P}, \tag{23}$$

where μ is dynamic viscosity and ΔP is the pressure drop across the pack. Within the model, the same Darcy framework is applied layerwise:

$$\Delta P_i = \mu u_D \frac{\Delta z}{k_i}, \quad \Delta P = \sum_{i=1}^{N} \Delta P_i \tag{24}$$

so that:

$$k_{eff} = \frac{H}{\sum_{i=1}^{N} \Delta z / k_i}. \tag{25}$$

This resistances-in-series structure is essential: it allows strong permeability reduction to be generated by clogging of only the upper layers, consistent with the post-experiment concentration profiles measured along the column height.

A constitutive relation is required to update k_i when particles are retained in layer i. The model uses a Kozeny–Carman-type closure in the form:

$$k_i = \frac{\phi_i^3}{c_K a_{s,i}^2}, \tag{26}$$

where $a_{s,i}$ is the specific surface area of the solid matrix (surface per bulk volume), and c_K is the Kozeny constant (or a generalized coefficient). This formulation makes explicit that permeability is controlled by both porosity and surface area and is therefore sensitive to throat narrowing and internal surface growth during deposition. For packed sands, $a_{s,i}$ can be initialized from the grain size scale (e.g., $a_s \sim 6(1-\phi)/d_g$ for spherical grains of characteristic diameter d_g); in real sands, d_g is taken as d_{50} (or another representative diameter from the measured granulometry), and c_K absorbs non-sphericity and packing effects.

Because nanoparticle retention modifies the void space, the model updates porosity through a deposited-volume balance. Let σ_i be the cumulative deposited mass per unit cross-section stored in layer i. The corresponding deposited bulk volume in that layer is σ_i/ρ_{dep}, where ρ_{dep} is an effective bulk density of the deposit (typically lower than the crystal density because deposits are porous/aggregated). The porosity update is:

$$\phi_i = \phi_0 - \frac{\sigma_i}{\rho_{dep}\Delta z} \tag{27}$$

with ϕ_0 the initial porosity of the clean pack. This is the minimum model needed to translate accumulated mass into an evolving flow cross-section. In practice, ρ_{dep} is a calibration parameter that implicitly accounts for aggregation state and deposit packing, and it strongly controls how quickly permeability declines for a given σ_{inj}.

To connect deposition to a throat length scale used in detachment physics, the model uses the hydraulic radius definition $r_{h,i} = \phi_i/a_{s,i}$. This choice is convenient because it remains meaningful for non-cylindrical pore shapes and automatically couples to the Kozeny relation. The throat radius $r_{t,i}$ used as a "hydraulic equivalent" scale is then taken proportional to $r_{h,i}$ (e.g., $r_{t,i} \sim O(r_{h,i})$; for sands in the 0.316–0.20 mm range this scale is typically tens of micrometers, and for 0.20–0.10 mm sands it is smaller but still much larger than the primary nanoparticle size, implying that retention is dominated by attachment/aggregation and flow-driven restructuring rather than simple geometric sieving. This is consistent with pore-scale and pore-network analyses showing that clogging is often governed by collective deposition/bridging and flow redistribution rather than only particle size cut-off [38].

Each increment $\Delta\sigma_{inj}$ enters the top layer as mobile mass $\Delta\sigma_{in}^{(1)}$. In each layer, a fraction is retained and the remainder is transmitted to the next layer:

$$\Delta\sigma_{dep}^{(i)} = \eta_i \Delta\sigma_{in}^{(i)}, \quad \Delta\sigma_{in}^{(i+1)} = \Delta\sigma_{in}^{(i)} - \Delta\sigma_{dep}^{(i)} + \Delta\sigma_{rel}^{(i)}, \tag{28}$$

here η_i is an effective capture efficiency for layer i, and $\Delta\sigma_{rel}$ is the mass released from previously deposited material in that layer during the same step (remobilization). This retention–release structure is standard in colloid transport modeling and is required to represent both clogging and subsequent stabilization regimes [39].

The choice of η_i is what makes the model reproduce the experimentally observed top-loaded retention. In a strictly homogeneous medium with constant η, retention would distribute exponentially with depth, which is not sufficient when deposition is confined to the upper centimeters. To enforce a finite clogging zone that grows downward only after an upstream layer reaches a local equilibrium, η_i is modeled

as a product of an inlet-biased attachment term and a hydrodynamic self-limiting term:

$$\eta_i = \eta_0 \exp(-\alpha z_i)\Psi\left(\frac{\tau_{w,i}}{\tau_c}\right)\Omega\left(\frac{\sigma_i}{\sigma_{eq,i}}\right). \quad (29)$$

The parameter η_0 sets the baseline propensity for retention at the inlet; α controls how rapidly this propensity decays with depth (capturing, in an effective way, the combined effects of particle depletion, aggregation and early capture). The function $\Omega(\sigma_i/\sigma_{eq,i})$ decreases from ≈ 1 at low deposit load to ≈ 0 when the layer reaches its equilibrium deposit capacity $\sigma_{eq,i}$, at which point additional injected mass is largely transmitted to deeper layers; this is the mechanism that produces a sharp advancing front. The hydrodynamic factor $\Psi(\tau_{w,i}/\tau_c)$ accounts for release: as wall shear approaches a critical value, net retention is reduced and can become negative (net erosion). The need for such a balance is well documented in experiments and models where colloid retention and release depend on flow velocity and surface roughness [40–42].

To compute Ψ, the model must estimate the characteristic wall shear stress in each layer. Using the capillary-bundle analogy for a porous medium, the shear at the pore wall scales with the pressure gradient times a hydraulic length. A convenient expression is:

$$\tau_{w,i} \approx \frac{r_{h,i}}{2}\left|\frac{\Delta P_i}{\Delta z}\right| = \left|\frac{r_{h,i}}{2}\frac{\mu u_D}{k_i}\right|. \quad (30)$$

This formula is consistent with laminar tube flow where $\tau_w = (R/2)\partial p/\partial x$, while $r_{h,i}$ plays the role of an effective radius. It directly embeds the key feedback: as deposition reduces k_i, the local pressure gradient increases, which increases $\tau_{w,i}$, which in turn enhances release and limits further build-up. The critical shear stress τ_c is treated as an effective parameter reflecting adhesive forces between deposits and the grain surface (including roughness, chemical interactions, and deposit structure). In neutral pH tap water without surfactants, τ_c is expected to depend strongly on surface roughness and on whether particles are retained in primary/secondary minima and by mechanical interlocking; this dependence motivates treating τ_c as a calibration parameter rather than a purely DLVO-derived value [41, 42].

A simple and numerically robust choice for the hydrodynamic factor is a piecewise function:

$$\Psi\left(\frac{\tau_{w,i}}{\tau_c}\right) = \begin{cases} 1 - \left(\frac{\tau_{w,i}}{\tau_c}\right)^m, & \tau_{w,i} \geq \tau_c, \\ -\chi\left[\left(\frac{\tau_{w,i}}{\tau_c}\right)^m - 1\right], & \tau_{w,i} \geq \tau_c, \end{cases} \quad (31)$$

where m controls how sharply retention weakens near the threshold, and χ scales how efficiently deposits are eroded once $\tau_{w,i}$ exceeds τ_c. This captures the experimentally observed transition from monotonic permeability decline to a late-stage stabilization where incremental injected mass mostly passes through without further net loss of permeability.

The equilibrium capacity $\sigma_{eq,i}$ is the deposited mass per area that a layer can sustain under the prevailing hydrodynamic conditions before release balances further capture. In the model it can be expressed implicitly by the condition of zero net accumulation:

$$\eta_i(\sigma_i = \sigma_{eq,i}) \approx 0 \Rightarrow \Omega(1) \approx 0 \text{ and/or } \Psi(\tau_{w,i}/\tau_c) \approx 0. \quad (32)$$

Physically, two mechanisms contribute: geometric limitation (available pore volume is reduced), and hydrodynamic limitation (shear-driven rearrangement and erosion intensify as k_i decreases). This equilibrium concept is consistent with experimental evidence that colloid retention and clogging are controlled by both solution chemistry and flow velocity, and that release can be triggered or enhanced by hydrodynamic forcing [40].

Once the uppermost layers reach $\sigma_{eq,i}$, the incoming mass is transmitted deeper, and the stable contamination front advances downward. In a discrete model this front depth z_f can be defined operationally as the deepest layer where σ_i exceeds a small fraction of its equilibrium value (e.g., $\sigma_i/\sigma_{eq,i} > \varepsilon$). The specific injected mass required to advance the front to depth z_f is then approximately:

$$\sigma_{\text{req}}(z_f) \approx \sum_{z_i \leq z_f} \sigma_{eq,i} \quad (33)$$

which directly provides the sought specific particle consumption needed to block a given thickness of porous medium under the tested hydraulic regime. This quantity is the natural bridge from laboratory columns to field injection: it is expressed per unit cross-sectional area, does not depend on column diameter, and can be reformulated per unit well screen area or per unit aquifer thickness.

The model contains a limited set of parameters, each with a clear physical role. The initial porosity ϕ_0 sets the clean permeability level together with the grain size scale and the Kozeny coefficient; it is chosen from the gravimetric packing state (mass, volume, and grain density) and/or from the clean-water permeability. The representative grain diameter d_g is selected from the measured granulometry (typically d_{50} for each sand fraction), while c_K is calibrated using the initial permeability and porosity for that fraction [35]. The deposit bulk density ρ_{dep} controls how rapidly porosity and hydraulic radius decline with retained mass; it is fitted so that the slope of $k(\sigma_{\text{inj}})$ in the long quasi-linear regime matches the experiments. The inlet-bias parameters η_0 and α determine how strongly deposition is concentrated near the top; they are constrained by the measured post-experiment vertical profiles of retained mass. The hydrodynamic parameters τ_c, m, and χ control when and how stabilization occurs; they are constrained by the onset of plateauing in the permeability curves and by differences between particle types and sands. Notably, smaller and denser particles (WO_3, 80–100 nm) are observed to penetrate deeper than TiO2 under otherwise comparable conditions, which in the model corresponds to either a smaller effective η_0 (lower net attachment), a smaller α (weaker inlet localization), a smaller ρ_{dep} (more open deposits), and/or a lower τ_c (more readily eroded deposits), consistent with the documented sensitivity of retention/release to surface roughness and hydrodynamic torques [40, 41].

The discretization thickness Δz is chosen as a compromise between capturing the observed localization (top centimeters) and maintaining numerical stability. Here $\Delta z = 5$ mm yields 40 layers, which is sufficient to reproduce sharply localized retention while keeping parameter identification tractable. The mass step $\Delta\sigma_{\text{inj}}$ is selected to match the experimental sampling resolution used for permeability evaluation; smaller steps improve smoothness but are not required if the model functions Ψ and Ω are continuous.

Model parameters are identified by simultaneous matching of two independent observables: the measured permeability decline as a function of cumulative injected mass per area, and the measured post-experiment retained mass distribution along the height of the pack (Fig. 4). Figure 4

(left side) shows k_{eff} versus σ_{inj} for all runs (different sands and particle types) together with the simulated curves; the model reproduces the extended near-linear decline regime followed by late-stage stabilization, which cannot be captured by a single exponential function. Figure 4 (right side) shows the simulated vertical distribution of retained mass (layerwise $\sigma_i/\Delta z$) compared with the measured concentration profile from the sectioned sand pack; the agreement confirms that the model reproduces the experimentally observed confinement of deposits to the upper portion of the column and the deeper penetration for WO_3 compared to TiO_2. These two matches jointly constrain both the hydraulic feedback (through k_i and $\tau_{w,i}$) and the transport/retention structure (through η_i, α, and $\sigma_{eq,i}$), reducing non-uniqueness.

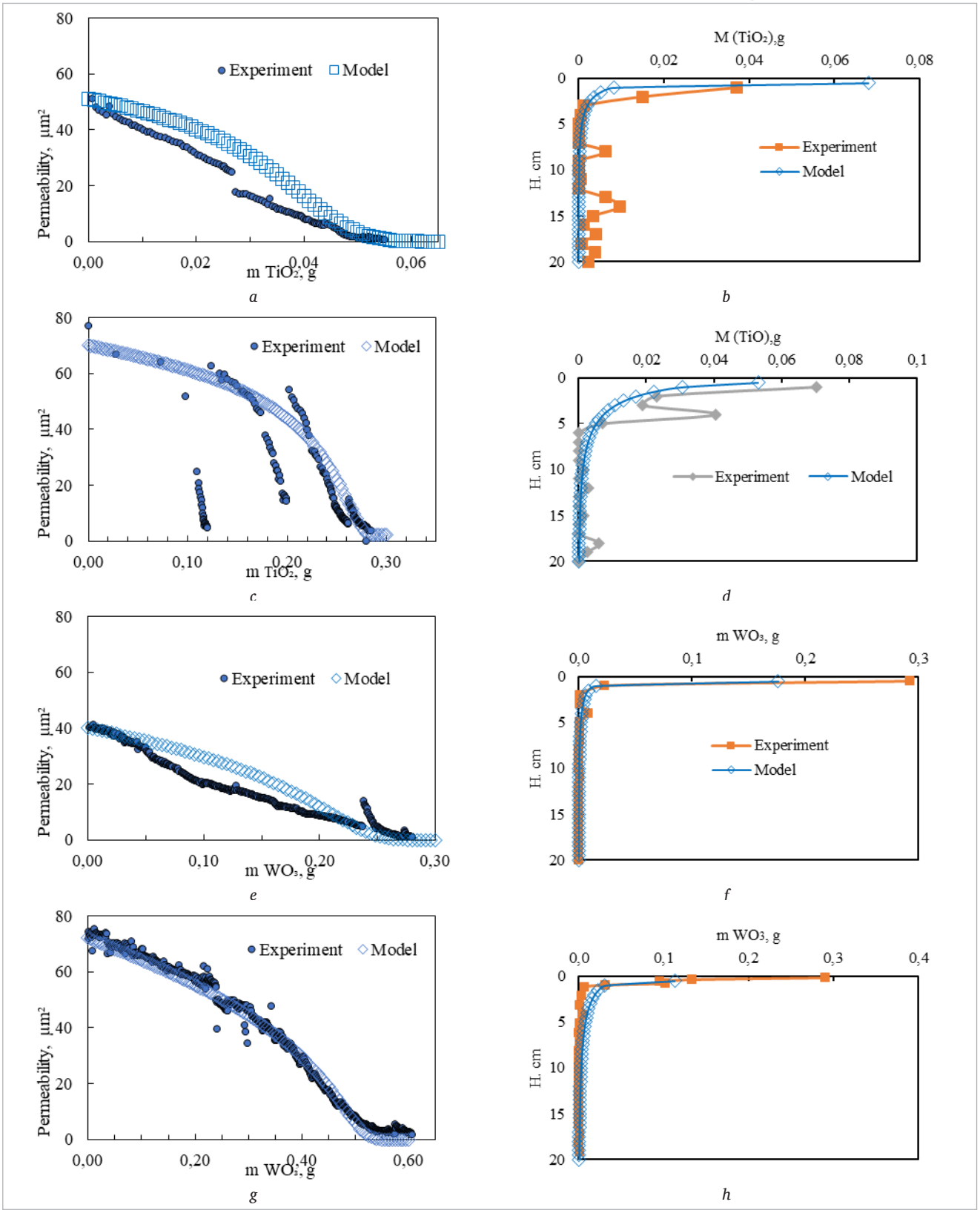


Fig. 4. Comparison of experimental and modelled results for permeability evolution (left) and retained-mass distribution along model height (right) for sand grain-size fractions: *a*, *b* – 0.2–0.1 mm; *c*, *d* – 0.316–0.2 mm; *e*, *f* – 0.2–0.1 mm, and *g*, *h* – 0.316–0.2 mm

Transfer of the Approach to Field Clogging in Injection and Recharge Wells

The proposed framework is directly transferable to near-wellbore clogging problems because it is formulated in terms of Darcy-scale resistance in series and mass per unit area required to create a stable clogged zone. In managed aquifer recharge and recharge wells, clogging is routinely driven by suspended solids, colloids, and fines migration; operationally, permeability decline and injectivity loss are often controlled by accumulated load and by hydrodynamic conditions, with stabilization or partial recovery possible under changing gradients and backwashing [43–45]. In subsurface disposal or reinjection of impaired waters (e.g., produced water, treated wastewater), similar physical clogging mechanisms coexist with chemical and biological effects; however, even in the presence of additional processes, a layer-based resistance model remains a practical backbone for quantifying the physical component of injectivity decline [46].

For field application, the one-dimensional layered column is mapped to a radial system by replacing layers by concentric shells around the wellbore (or by discretizing the formation thickness vertically if stratification dominates). The same core elements are retained: local permeability evolves with deposited mass, the pressure gradient increases where permeability is reduced, and a dynamic deposition–release equilibrium defines a growing clogged zone. The key scaling variable σ_{inj} is then interpreted as mass per unit inflow area (screen area, borehole wall area, or the effective inflow area at the formation face). Grain size and porosity are taken from cores, cuttings, or logs, and c_K is calibrated on baseline permeability. Particle size distributions are taken from water quality monitoring, and the parameters controlling η and τ_c are tuned using step-rate tests, injectivity decline curves, and (where available) depth-resolved solids profiling.

Finally, extrapolation to less permeable consolidated sandstones follows naturally from the geometric closure: smaller hydraulic radius and lower baseline permeability imply larger pressure gradients at the same flux, hence larger τ_w and a different equilibrium between deposition and release. At the same time, the particle-to-throat size ratio increases, so straining and bridging may become more important, and the effective deposit density ρ_{dep} may increase due to tighter confinement. Pore-network studies explicitly show that pore structure controls where and how clogging localizes and how flow redistributes, supporting the need to re-identify η_0, α, and σ_{eq} when moving from unconsolidated packs to consolidated pore networks [38].

Overall, the discrete 5-mm layered formulation provides the minimum level of spatial resolution required to reproduce the localization of deposits near the inlet, the downward advance of a stable clogged zone as cumulative mass increases, and the late-stage stabilization of permeability due to a deposition–release balance that is controlled by local wall shear stress and deposit properties.

Conclusions

Injectivity decline caused by suspended solids remains a critical operational risk for water injection and recharge systems; the findings of this study can be summarized as follows:

1. Permeability impairment is primarily governed by particulate loading: permeability decreases rapidly at early stages of submicron particle injection and then approaches a weak-sensitivity regime, consistent with preferential blockage of the most conductive flow paths followed by flow redistribution.

2. The pore-throat scale controls clogging susceptibility: finer granular packs exhibit stronger and earlier permeability loss than coarser packs, reflecting the greater vulnerability of smaller constrictions to obstruction by submicron particles.

3. Submicron particle size influences penetration and the loading required to reach comparable damage: smaller particles tend to penetrate deeper into the porous structure and generally require a higher injected mass to produce the same overall permeability reduction, indicating lower near-inlet retention efficiency and enhanced transport.

4. Deposition is spatially localized near the inlet: retained mass profiles are strongly inlet-biased, with the main deposited load concentrated in the upper portion of the pack and decreasing with depth, implying that a shallow high-resistance zone largely controls the macroscopic flow response.

5. A layer-resolved, resistance-based description is suitable for upscaling: representing the medium as thin layers with evolving local resistance captures both the overall permeability trend and the depth-wise retention pattern, providing a practical basis for transferring laboratory observations to near-wellbore clogging in injection, disposal, and recharge wells.

References

1. Liu, W.; He, H.; Yuan, F.; Liu, H.; Zhao, F.; Liu, H.; Luo, G. Influence of the Injection Scheme on the Enhanced Oil Recovery Ability of Heterogeneous Phase Combination Flooding in Mature Waterflooded Reservoirs. ACS Omega 2022, 7, 23511–23520, doi:10.1021/acsomega.2c02007.
2. Wang, Y.; Almutairi, A.L.Z.; Bedrikovetsky, P.; Timms, W.A.; Privat, K.L.; Bhattacharyya, S.K.; Le-Hussain, F. In-Situ Fines Migration and Grains Redistribution Induced by Mineral Reactions – Implications for Clogging during Water Injection in Carbonate Aquifers. J. Hydrol. (Amst). 2022, 614, 128533, doi:10.1016/j.jhydrol.2022.128533.
3. Borazjani, S.; Behr, A.; Genolet, L.; Van Der Net, A.; Bedrikovetsky, P. Effects of Fines Migration on Low-Salinity Waterflooding: Analytical Modelling. Transp. Porous Media 2017, 116, 213–249, doi:10.1007/s11242-016-0771-2.
4. Yang, Y.; Yuan, W.; Hou, J.; You, Z. Review on Physical and Chemical Factors Affecting Fines Migration in Porous Media. Water Res. 2022, 214, 118172, doi:10.1016/j.watres.2022.118172.
5. Wang, C.; Wang, R.; Huo, Z.; Xie, E.; Dahlke, H.E. Colloid Transport through Soil and Other Porous Media under Transient Flow Conditions—A Review. WIREs Water 2020, 7, doi:10.1002/wat2.1439.
6. Attabi, K.A.L.; Altalbawy, F.M.A.; Hassan, H.I.; Sahib, A.S.; Abdulali, Z.S.; Alwan, M.; Jawad, M.; Mushtaq, H.; Smerat, A.; Khalid, A. Mitigation of Fine Migration in Low Salinity Water Flooding of Clay-Rich Sandstones Using Fe_3O_4/Saponin/Cu(II) Nanocomposite. Discover Nano 2026, 21, 18, doi:10.1186/s11671-026-04441-9.
7. Russell, T.; Pham, D.; Neishaboor, M.T.; Badalyan, A.; Behr, A.; Genolet, L.; Kowollik, P.; Zeinijahromi, A.; Bedrikovetsky, P. Effects of Kaolinite in Rocks on Fines Migration. J. Nat. Gas Sci. Eng. 2017, 45, 243–255, doi:10.1016/j.jngse.2017.05.020.
8. Shulkin, V.M. USE OF THE DYNAMIC LIGHT SCATTERING TO ASSESS THE EFFICIENCY OF SEPARATION OF SUSPENDED AND COLLOIDAL PARTICLES IN RIVER WATERS BY FILTRATION AND CENTRIFUGATION. Bulletin of the Tomsk Polytechnic University Geo Assets Engineering 2023, 334, 88–97, doi:10.18799/24131830/2023/10/4095.
9. Cheng, W.; Xi, H.; Chen, Y.; Zhao, X.; Zhao, J.; Ma, K. Infiltration Mechanism of the Sandy Riverbed in the Arid Inland Region of China. J. Hydrol. Reg. Stud. 2022, 42, 101145, doi:10.1016/j.ejrh.2022.101145.
10. Hannun, J.A.; Al-Raoush, R.I.; Jarrar, Z.A.; Alshibli, K.A.; Jung, J. Fines Effect on Gas Flow in Sandy Sediments Using MCT and Pore Networks. J. Nat. Gas Sci. Eng. 2022, 108, 104834, doi:10.1016/j.jngse.2022.104834.

11. Yin, Y.; Cui, Y.; Jing, L. Clogging and Unclogging of Fine Particles in Porous Media: Micromechanical Insights From an Analog Pore System. Water Resour. Res. 2024, 60, DOI:10.1029/2023WR034628.
12. Almutairi, A.; Saira, S.; Wang, Y.; Le-Hussain, F. Effect of Fines Migration on Oil Recovery from Carbonate Rocks. Advances in Geo-Energy Research 2023, 8, 61–70, DOI:10.46690/ager.2023.04.06.
13. Zhai, X.; Atefi-Monfared, K. Production versus Injection Induced Poroelasticity in Porous Media Incorporating Fines Migration. J. Pet. Sci. Eng. 2021, 205, 108953, doi:10.1016/j.petrol.2021.108953.
14. Bagrezaie, M.A.; Dabir, B.; Rashidi, F. A Novel Approach for Pore-Scale Study of Fines Migration Mechanism in Porous Media. J. Pet. Sci. Eng. 2022, 216, 110761, doi:10.1016/j.petrol.2022.110761.
15. Bedrikovetsky, P.; Vaz, A.; Machado, F.; Zeinijahromi, A.; Borazjani, S. Skin Due to Fines Mobilization, Migration, and Straining During Steady-State Oil Production. Pet. Sci. Technol. 2012, 30, 1539–1547, doi:10.1080/10916466.2011.653702.
16. Yang, Y.; Bedrikovetsky, P. Exact Solutions for Nonlinear High Retention-Concentration Fines Migration. Transp. Porous Media 2017, 119, 351–372, doi:10.1007/s11242-017-0885-1.
17. Zhai, X.; Atefi-Monfared, K. Injection-Induced Poroelastic Response of Porous Media Containing Fine Particles, Incorporating Particle Mobilization, Transport, and Straining. Transp. Porous Media 2021, 137, 629–650, doi:10.1007/s11242-021-01580-8.
18. Wendling, P.; Curtis, J.S.; Nirschl, H.; Gleiss, M. Microstructure Simulation to Predict the Influence of Particle Properties on Permeability of Granular Porous Media. Transp. Porous Media 2026, 153, 18, doi:10.1007/s11242-025-02267-0.
19. Vyas, D.R.; Gao, S.; Umbanhowar, P.B.; Ottino, J.M.; Lueptow, R.M. Impacts of Packed Bed Polydispersity and Deformation on Fine Particle Transport. AIChE Journal 2024, 70, doi:10.1002/aic.18499.
20. Dersoir, B.; Schofield, A.B.; Robert de Saint Vincent, M.; Tabuteau, H. Dynamics of Pore Fouling by Colloidal Particles at the Particle Level. J. Memb. Sci. 2019, 573, 411–424, doi:10.1016/j.memsci.2018.12.025.
21. Okaybi, W.; Roman, S.; Soulaine, C. Progressive Colloidal Clogging Mechanism by Dendritic Build-up in Porous Media. Soft Matter 2025, 21, 5687–5698, doi:10.1039/D5SM00285K.
22. Han, G.; Kwon, T. Effect of Seepage Velocity on Pore Clogging Growth Behavior and Its Effect on Permeability Reduction During Fines Migration in Porous Media. Water Resour. Res. 2023, 59, doi:10.1029/2022WR033537.
23. Al-Zghoul, B.M.; Volponi, S.N.; Johnson, W.P.; Bolster, D. Effects of Initial Injection Condition on Colloid Retention. Water Resour. Res. 2024, 60, doi:10.1029/2023WR036877.
24. Jung, J.; Cao, S.C.; Shin, Y.-H.; Al-Raoush, R.I.; Alshibli, K.; Choi, J.-W. A Microfluidic Pore Model to Study the Migration of Fine Particles in Single-Phase and Multi-Phase Flows in Porous Media. Microsystem Technologies 2018, 24, 1071–1080, doi:10.1007/s00542-017-3462-1.
25. Soulaine, C.; Pavuluri, S.; Claret, F.; Tournassat, C. PorousMedia4Foam: Multi-Scale Open-Source Platform for Hydro-Geochemical Simulations with OpenFOAM®. Environmental Modelling & Software 2021, 145, 105199, doi:10.1016/j.envsoft.2021.105199.
26. Xu, Y.; Ye, X.; Du, X. Microscopic Mechanism of Particle Clogging in Porous Media During Managed Aquifer Recharge: From X-Ray Computed Tomography (<scp>CT</scp>) Imaging to Numerical Modelling. Hydrol. Process. 2024, 38, doi:10.1002/hyp.70002.
27. Liu, Q.; Zhao, B.; Santamarina, J.C. Particle Migration and Clogging in Porous Media: A Convergent Flow Microfluidics Study. J. Geophys. Res. Solid Earth 2019, 124, 9495–9504, doi:10.1029/2019JB017813.
28. You, Z.; Badalyan, A.; Yang, Y.; Bedrikovetsky, P.; Hand, M. Fines Migration in Geothermal Reservoirs: Laboratory and Mathematical Modelling. Geothermics 2019, 77, 344–367, doi:10.1016/j.geothermics.2018.10.006.
29. Haoxuan, T.; Chunsheng, J.; Ziyi, W.; Hao, L.; Zhao, W.; Hongming, T.; Baiyu, Z. Evolution of Pore Structure during Fines Migration in Sand Pack: NMR Experimental and Numerical Investigations. Front. Energy Res. 2024, 12, doi:10.3389/fenrg.2024.1399477.
30. Wang, Z.; Yin, H.; Tang, H.; Hou, Y.; Yu, H.; Liu, Q.; Tang, H. Analysis of Damage Mechanisms and Controlling Factors of Fine Particle Migration in Unconsolidated Sandstone Reservoirs Based on Reservoir Classification. Energy Sci. Eng. 2024, 12, 2879–2898, doi:10.1002/ese3.1781.
31. Kottsova, A.K.; Mirzaie Yegane, M.; Tchistiakov, A.A.; Zitha, P.L.J. Effect of Electrostatic Interaction on the Retention and Remobilization of Colloidal Particles in Porous Media. Colloids Surf. A Physicochem. Eng. Asp. 2021, 617, 126371, doi:10.1016/j.colsurfa.2021.126371.
32. Cui, R.; Page, D.; Du, X.; Zhang, H.; Ye, X. Effect of Iron on Biological Clogging in Porous Media: Implications for Managed Aquifer Recharge. Hydrol. Process. 2023, 37, doi:10.1002/hyp.14839.
33. Zhai, X.; Atefi-Monfared, K. Novel Modeling of Non-Isothermal Flow-Induced Fine Particle Migration in Porous Media Based on the Derjaguin-Landau-Verwey-Overbeek Theory. Transp. Porous Media 2024, 151, 1983–2015, doi:10.1007/s11242-024-02103-x.
34. Al-Sarihi, A.; Zeinijahromi, A.; Genolet, L.; Behr, A.; Kowollik, P.; Bedrikovetsky, P. Effects of Fines Migration on Residual Oil during Low-Salinity Waterflooding. Energy & Fuels 2018, 32, 8296–8309, doi:10.1021/acs.energyfuels.8b01732.
35. Xu, P.; Yu, B. Developing a New Form of Permeability and Kozeny–Carman Constant for Homogeneous Porous Media by Means of Fractal Geometry. Adv. Water Resour. 2008, 31, 74–81, doi:10.1016/j.advwatres.2007.06.003.
36. Costa, A. Permeability-porosity Relationship: A Reexamination of the Kozeny-Carman Equation Based on a Fractal Pore-space Geometry Assumption. Geophys. Res. Lett. 2006, 33, doi:10.1029/2005GL025134.
37. Heijs, A.W.J.; Lowe, C.P. Numerical Evaluation of the Permeability and the Kozeny Constant for Two Types of Porous Media. Phys. Rev. E 1995, 51, 4346–4352, doi:10.1103/PhysRevE.51.4346.
38. Lin, D.; Hu, L.; Bradford, S.A.; Zhang, X.; Lo, I.M.C. Simulation of Colloid Transport and Retention Using a Pore-Network Model With Roughness and Chemical Heterogeneity on Pore Surfaces. Water Resour. Res. 2021, 57, doi:10.1029/2020WR028571.
39. Molnar, I.L.; Johnson, W.P.; Gerhard, J.I.; Willson, C.S.; O'Carroll, D.M. Predicting Colloid Transport through Saturated Porous Media: A Critical Review. Water Resour. Res. 2015, 51, 6804–6845, doi:10.1002/2015WR017318.
40. Torkzaban, S.; Bradford, S.A.; Vanderzalm, J.L.; Patterson, B.M.; Harris, B.; Prommer, H. Colloid Release and Clogging in Porous Media: Effects of Solution Ionic Strength and Flow Velocity. J. Contam. Hydrol. 2015, 181, 161–171, doi:10.1016/j.jconhyd.2015.06.005.
41. Torkzaban, S.; Bradford, S.A. Critical Role of Surface Roughness on Colloid Retention and Release in Porous Media. Water Res. 2016, 88, 274–284, doi:10.1016/j.watres.2015.10.022.
42. Bradford, S.A.; Torkzaban, S. Determining Parameters and Mechanisms of Colloid Retention and Release in Porous Media. Langmuir 2015, 31, 12096–12105, doi:10.1021/acs.langmuir.5b03080.
43. Zhang, H.; Xu, Y.; Kanyerere, T. A Review of the Managed Aquifer Recharge: Historical Development, Current Situation and Perspectives. Physics and Chemistry of the Earth, Parts A/B/C 2020, 118–119, 102887, doi:10.1016/j.pce.2020.102887.
44. Fernández Escalante, E. Practical Management to Minimize the Effects of Clogging in Managed Aquifer Recharge Wells at Two Sites in the Guadiana Basin, Spain. J. Hydrol. Eng. 2015, 20, doi:10.1061/(ASCE)HE.1943-5584.0001047.
45. Kalwa, F.; Binder, M.; Händel, F.; Grüneberg, L.; Liedl, R. Biological and Physical Clogging in Infiltration Wells: Effects of Well Diameter and Gravel Pack. Groundwater 2021, 59, 819–828, doi:10.1111/gwat.13104.
46. Du, X.; Ye, X.; Zhang, X. Clogging of Saturated Porous Media by Silt-sized Suspended Solids under Varying Physical Conditions during Managed Aquifer Recharge. Hydrol. Process. 2018, 32, 2254–2262, doi:10.1002/hyp.13162.

Acknowledgments. The study was supported by a grant from the Russian Science Foundation No. 25-79-10350, https://rscf.ru/project/25-79-10350.
Conflict of interests. The authors declare that there is no conflict of interest.
The contribution of the authors is equivalent.

Финансирование. Исследование было поддержано грантом Российского научного фонда № 25-79-10350, https://rscf.ru/project/25-79-10350.
Конфликт интересов. Авторы заявляют об отсутствии конфликта интересов.
Вклад авторов равнозначен.